Ferromagnetic exchange in a twisted, oxime-bridged [Mn(III)2] dimer

Dalton Transactions

Dynamic Article Links ►

Cite this: 2012, 41(27), 8340-8347

www.rsc.org/xxxxxx

Full paper

Ferromagnetic exchange in a twisted, oxime-bridged [Mn^{III}_2] dimer

Edel Houton,[a] Stephanie M. Taylor,[b] Christopher C. Beedle,[c] Joan Cano,[d] Stergios Piligkos,[e] Stephen Hill,[c] Alan G. Ryder,*[a] Euan K. Brechin*[b] and Leigh F Jones*[a]

Received (in XXX, XXX) Xth XXXXXXXXX 20XX, Accepted Xth XXXXXXXXX 20XX

DOI: 10.1039/b000000x

The dimeric complex [Mn^{III}_2(Naphth-sao)$_2$(Naphth-saoH)$_2$(MeOH)$_2$]·4MeOH (**1**·4MeOH), acts as a simple model complex with which to examine the magneto-structural relationship in polymetallic, oxime-bridged Mn^{III} complexes. Dc magnetic susceptibility studies reveal that ferromagnetic exchange is mediated through the heavily twisted Mn-O-N-Mn moiety (J = +1.24 cm^{-1}) with magnetisation measurements at low temperatures and high fields suggesting significant anisotropy. Simulations of high field, high frequency EPR data reveal a single ion anisotropy, $D_{(Mn^{III})}$ =-3.94 cm^{-1}. Theoretical studies on simplified model complexes of **1** reveal that calculated values of the exchange coupling and the anisotropy are in excellent agreement with experiment, with the weak ferromagnetism resulting from an accidental orthogonality between the Mn-N-O plane of the first Mn^{III} ion and the Jahn-Teller axis of the second Mn^{III} ion.

Introduction

The relationship between the structure of a molecule and its magnetic properties has fascinated chemists for decades.[1] For example, the relationship between the magnitude and sign of magnetic exchange in hydroxo-bridged Cu^{II} dimers was shown to be dependent on the Cu-O-Cu bridging angle,[2] while in complexes containing the [Cr^{III}(OH)]$_2$ core the dominant structural factor was the variation of the angle between the O-H vector and the Cr_2O_2 plane.[3] While more recent papers in molecular magnetism have concentrated on sub-topics such as (amongst others) single-molecule magnetism,[4] quantum information processing[5] and magnetic cooling,[6] they still all fundamentally rely on a detailed understanding and exploitation of the structure-property relationship. However as these early studies showed, this is not a trivial process and it becomes increasingly more difficult as the molecules increase in size, since the number of contributions to the exchange increases – this is particularly true for the 'giant' cluster compounds that have emerged in recent years containing tens, if not hundreds, of metal centres.[7]

The logical construction of (large) molecules exhibiting ferromagnetic or ferrimagnetic exchange is also a very difficult task. Target molecules often contain high-valent metal ions (*e.g.* Mn^{III}, Fe^{III} *etc*) and as such their cores are commonly constructed from oxide and/or hydroxide anions, whose presence, number and behaviour is difficult to control.[8] One alternative strategy is to make small molecules (dimers, trimers *etc*) whose structures can be manipulated to such an extent that the magnetic exchange between the metal ions can be controlled, and then to use these small molecules as the building blocks from which large or very large molecules (or indeed coordination polymers) with 'tailored' magnetic properties can be made.

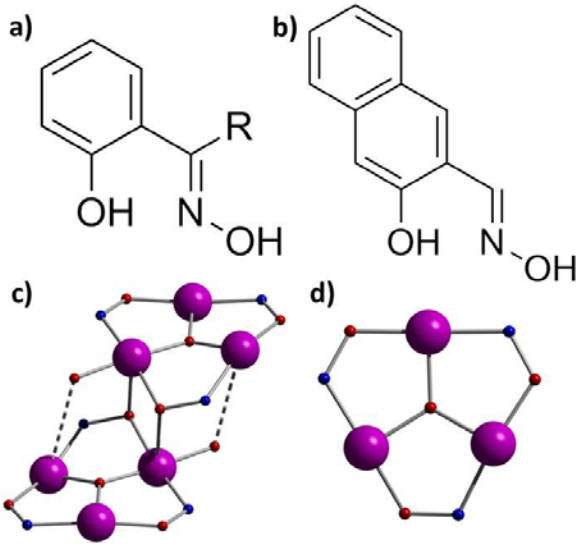

Scheme 1. (a) Generic structure of the phenolic oxime, R-saoH$_2$. (b) Naphth-saoH$_2$. Magnetic cores present in the complexes (c) [Mn^{III}_6] and (d) [Mn^{III}_3] whose magnetic exchange can be controlled by the structural distortion of the Mn-O-N-Mn moiety.

An appealing class of ligand for the construction of high spin Mn^{III} molecules are the phenolic oximes, R-saoH$_2$ (Scheme 1).[9] Previous studies of over eighty members of the [Mn(III)$_n$] (n = 3, 6) family of clusters stabilised with these ligands revealed a semi-quantitative magneto-structural correlation whose main conclusion was that the *dominant* structural factor dictating the pairwise magnetic exchange within the triangular unit was the twisting of the Mn-O-N-Mn moiety.[10] If the Mn-O-N-Mn torsion

angle was greater than ~31º the pairwise exchange was found to be ferromagnetic. Herein we continue our attempts to understand this relationship by reporting the serendipitous self-assembly of the dimeric complex $[Mn^{III}_2(Naphth\text{-}sao)_2(Naphth\text{-}saoH)_2(MeOH)_2]\cdot 4MeOH$ (**1**·4 MeOH) whose very simple magnetic core consists of only two symmetry equivalent Mn^{III} ions linked by two symmetry equivalent -N-O- moieties. We discuss its structure, magnetometry, EPR spectroscopy and a theoretical analysis of the magneto-structural relationship.

Experimental

Materials and physical measurements

All manipulations were carried out under aerobic conditions using materials as received (reagent grade). Naphth-saoH_2 was synthesised by the reaction of the precursor ketone with hydroxylamine and sodium acetate in EtOH, as described in the literature.[11] Elemental analyses (C, H, N) were performed at the School of Chemistry, NUI Galway. Variable-temperature, solid-state direct current (dc) magnetic susceptibility data down to 1.8 K were collected on a Quantum Design MPMS-XL SQUID magnetometer equipped with a 7 T dc magnet. Diamagnetic corrections were applied to the observed paramagnetic susceptibilities using Pascal's constants. Complex **1** was set in an eicosane wax to avoid torqueing of the crystallites.

FT-IR and Raman spectra were obtained at the Nanoscale Biophotonics Laboratory at the School of Chemistry, NUI Galway. Infra-red spectra were recorded on a Perkin Elmer FT-IR *Spectrum One* spectrometer equipped with a Universal ATR Sampling accessory. Raman measurements were recorded at room temperature using a Kaiser Optical Systems Raman spectrometer (*RamanRxn2^{TM} 1000 Analyzer*) equipped with a 993 nm laser diode excitation source and an InGaAs array detector. A laser power of ~200 mW (at the sample) with an exposure time of 10 × 8 seconds was used and spectra were collected from 250 to 4000 cm^{-1} (at a resolution of 5 cm^{-1}). Raman spectra of the coloured complex 1 was collected from a solid dispersion (approximately 1.5% by weight of complex) in dry KBr which was pressed into a disk using a hydraulic press and a 13 mm die set. This was done to minimise sample burning due to excessive absorption of excitation light. All data were normalised to the peak of maximum intensity and baseline corrected using standard methods.

Synthesis

$MnCl_2\cdot 4H_2O$ (0.25 g, 1.26 mmol), Naphth-saoH_2 (0.236 g, 1.26 mmol), Sodium 1-Napthoate (0.25 g, 1.26 mmol) and NaOMe (0.068 g, 1.26 mmol) were stirred in MeOH (30 cm^3) for 2 hours, filtered and allowed to stand. Black diamond shaped crystals of **1** were formed upon slow evaporation of the mother liquor in 15% yield over a period of 7 days. Elemental analysis (%) calculated (Found) for **1**·3H_2O: C 54.64 (54.73), H 4.49 (4.36), N 5.09 (5.44). FT-IR (cm^{-1}): 3383(vb), 1679(w), 1614(s), 1592(s), 1570(m), 1555(m), 1533(s), 1504(m), 1453(s), 1427(s), 1388(s), 1324(s), 1300(m), 1282(s), 1247(s), 1192(s), 1163(m), 1146(m), 1092(m), 1050(vs), 1029(m), 1014(w), 950(s), 926(w), 883(w), 865(m), 826(s), 776(s), 753(vs), 679(w). Raman spectrum (993 nm excitation) (cm^{-1}): 241(w), 236(w), 335(w), 354(w), 369(w), 428(w), 467(w), 505(m), 530(w), 556(w), 635(w), 650(s), 682(m), 761(m), 774(w), 879(w), 925(w), 957(w), 1028(m), 1049(w), 1091(w), 1142(w), 1194(m), 1215(w), 1247(w), 1377(s), 1427(w), 1427(s), 1454(m), 1528(m), 1564(w), 1591(w), 1614(w).

X-ray crystallography

The structure of **1** was collected on an Xcalibur S single crystal diffractometer (Oxford Diffraction) using an enhanced Mo source. Each data reduction was carried out on the CrysAlisPro software package. The structures were solved by direct methods (SHELXS-97)[12] and refined by full matrix least squares using SHELXL-97.[13] SHELX operations were automated using the OSCAIL software package.[14] All hydrogen atoms in **1** were modelled isotropically and assigned to idealised positions. Data collection parameters and structure solution and refinement details are given in Table S1. Full details can be found in the CIF file: CCDC XXXX.

Results and discussion

The reaction of $MnCl_2\cdot 4H_2O$, Naphth-saoH_2, Sodium 1-Napthoate and NaOMe in MeOH for 2 hours, followed by filtration and slow evaporation of the mother liquor affords black crystals of $[Mn^{III}_2(Naphth\text{-}sao)_2(Naphth\text{-}saoH)_2(MeOH)_2]\cdot 4MeOH$ (**1**·4MeOH; Figure 1). Although the carboxylate does not appear in the final product, its presence in the reaction mixture is required since no crystalline product is formed in its absence. **1** crystallises in the orthorhombic space group *Pbca*. The molecule describes a dimer of symmetry equivalent Mn ions which are six-coordinate and in Jahn-Teller (JT) distorted octahedral geometries with $[O_4N_2]$ coordination spheres. The JT axes are defined by the O2(oximic O)-Mn1-O5(MeOH) (and s.e.) vector (Mn1…O5, 2.333 Å; Mn1…O2, 2.197 Å). The oxime ligands are of two types: Naphth-sao^{2-} and Napth-saoH^{1-}. The former are μ-bridging linking the two Mn^{III} ions together *via* the (very twisted) -O-N- oxime linkage (Mn-O-N-Mn, 80.28°); the latter are simply chelating – one on each of the two Mn ions, with their protonated oximic O-arm (O4) H-bonded to a bridging oximic O-atom (O4…O2, 2.573 Å) and with a further longer contact to the terminally bonded phenolate O-atom (O4…O1, 3.404 Å). The sixth coordination site on the two Mn ions is completed by the presence of a terminally bonded MeOH molecule, and it is these and the terminally bonded phenolate O-atoms that propagate the extensive inter-molecular H-bonded interactions *via* the interstitial MeOH solvate molecules (Figure 1): the terminally bonded MeOH molecule (O5) is H-bonded to one MeOH of crystallisation (O5…O7, 2.654 Å), which in turn is H-bonded to a second MeOH molecule of crystallisation (O7…O6, 2.672 Å), which in turn is H-bonded to the two terminally bonded phenolate O-atoms on the neighbouring cluster molecule (O6…O1, 2.936 Å; O6…O3, 2.956 Å). The result is the formation of a H-bonded 2D sheet in the *ac* plane, with the inter-plane interactions occuring *via* the C-H···π interactions of the 'inter-digitated' naphthalene moieties, with typical C···centroid distances of 3.560 Å.

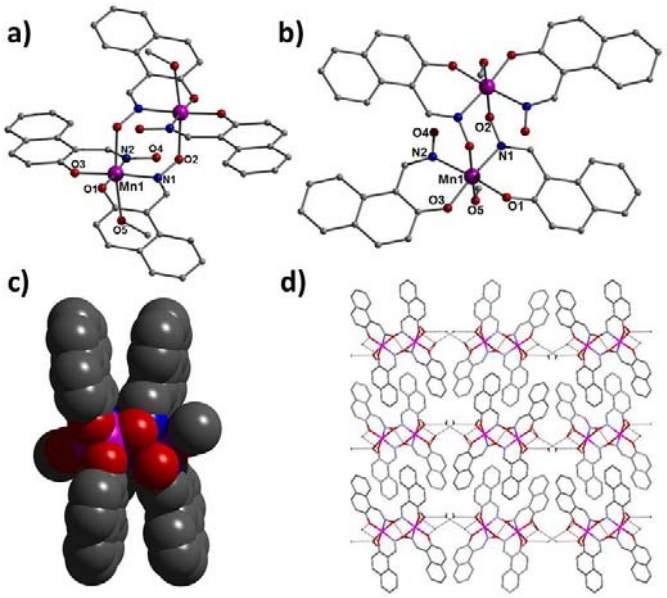

Figure 1 (a) and (b) Orthogonal views of the molecular structure of complex **1**. (c) Space filling diagram of **1**. (d) Packing of molecules of **1** in the crystal viewed down the *b*-axis. Colour code: Mn = purple, O = red, N = blue, C = grey. H-atoms and solvent molecules of crystallisation have been omitted for clarity.

Complex **1** is only the second example of an oxime-bridged Mn^{III} dimer and indeed is a very rare example of an oxime bridged Mn dimer at any oxidation level.[15] It's closest analogue is the heterometallic complex $[Mn^{III}_2Zn^{II}_2(Ph\text{-}sao)_2(Ph\text{-}saoH)_4(hmp)_2]$ (Hhmp = 2-hydroxymethylpyridine) we reported very recently, which also displays the very simple $[Mn^{III}(NO)]_2$ magnetic core.[15]

IR and Raman Studies

An extensive FT-IR and Raman analysis of complex **1** along with the Napth-saoH$_2$ ligand was undertaken using an adapted method of sample preparation (see experimental section for details), taking advantage of the C=N and N-O oxime functional groups (among others) within the bridging ligands in **1**. To this end IR (*weak*) and Raman (*strong and sharp*) bands were observed in the 1587-1614 cm^{-1} and 1368-1379 cm^{-1} regions respectively (Fig. S5 and Fig. S6) and attributed to multiple aromatic ν(C=C) stretching vibrations as expected for complex **1**.[16] The bands centred at 1633 cm^{-1} may be tentatively attributed to the ν(C=N) oxime stretching mode, as observed elsewhere.[17] Attempts at assigning the ν(N-O) stretching modes in Napth-saoH$_2$ and **1** were severely hampered by the significant spectral overlap in the 900-1150 cm^{-1} region of both the IR and Raman spectra (Fig. S1 and Fig. S2). Previous reports on ligating aromatic oximes have documented ν(N-O) stretching IR bands in the ~1050-1250 cm^{-1} spectral range and so should be considered here.[18] A full report on these findings is given in the ESI.

SQUID magnetometry

Dc magnetic susceptibility measurements were performed on a powdered microcrystalline sample of **1** in an applied magnetic field of 0.1 T and in the temperature range 275 to 5 K. The results are plotted as the $\chi_M T$ product vs. T in the top panel of Figure 2. The high temperature $\chi_M T$ value of 5.92 cm^3 K mol^{-1} is very close to that expected from the spin-only value (6.00 cm^3 K mol^{-1}) for two non-interacting high-spin Mn^{III} ($3d^4$) ions, assuming g = 2. This value increases constantly as the temperature is decreased, reaching a maximum of 9.66 cm^3 K mol^{-1} at 6 K before decreasing slightly to a value of 9.60 cm^3 K mol^{-1} at 5 K. This behaviour is indicative of the presence of an intra-molecular ferromagnetic exchange interaction between the two Mn^{III} ions. The small drop in the $\chi_M T$ product below 6 K is ascribed to inter-molecular interactions and/or zero-field splitting of the ground spin-state. For the interpretation of the magnetic properties of **1** we employed the isotropic spin-Hamiltonian (1):

$$\hat{H} = -2J\hat{S}_1 \cdot \hat{S}_2 + \sum_{i=1,2}\{\mu_B \vec{B} g \hat{S}_i\} \qquad (1)$$

where J is the isotropic exchange interaction parameter, $\hat{S}$ is a spin-operator, i = 1, 2, μ_B is the Bohr magneton, $\vec{B}$ is the applied magnetic field vector, and g = 2.00 is the g-factor of the Mn^{III} ions. The $\chi_M T$ product of **1** was numerically fitted, by use of the simplex algorithm,[19] to this spin-Hamiltonian by numerical diagonalisation of the full spin-Hamiltonian matrix. The best fit parameter was J = +1.24 cm^{-1}, affording an S = 4 ground state, with the first excited state (S = 3) approximately 10 cm^{-1} higher in energy. In addition, inter-molecular interactions were taken into account in the frame of mean-field theory, by use of the Curie–Weiss temperature, θ. A Curie-Weiss constant of θ = -0.54 K, was necessary to reproduce the small drop of the $\chi_M T$ product below 6 K. Inclusion of axial anisotropy to the above isotropic spin-Hamiltonian did not increase the quality of fit in a significant way (f-test of 0.97), leaving the J and θ parameters essentially unaltered, and resulted in a relatively low best-fit single-ion axial anisotropy (-0.55 cm^{-1}) for the Mn^{III} centres. This is not surprising since anisotropy effects are predominant at very low temperatures and thus, do not weight significantly in the fitting of the $\chi_M T$ product of **1**.

The ferromagnetic nature of the exchange between the two metals, mediated *via* the oximate -N-O- bridges, was expected on the basis of previous magneto-structural correlations in phenolic oxime based $[Mn^{III}_3]$ and $[Mn^{III}_6]$ clusters that have suggested that Mn-N-O-Mn torsion angles above approximately 31° are likely to result in ferromagnetic pairwise exchange.[20] The magnitude of the exchange is also similar to that seen in the complex $[Mn^{III}_2Zn^{II}_2(Ph\text{-}sao)_2(Ph\text{-}saoH)_4(hmp)_2]$.[15]

In order to determine the single-ion axial anisotropy parameter for the Mn^{III} centres in **1**, variable-temperature-variable-field dc magnetisation experiments were performed in the 2.0–7.0 K and 0.5–5.0 T temperature and magnetic field ranges, respectively. These experimental data are presented as reduced magnetisation ($M/N\mu_B$ *vs.* $\mu_B B/kT$, with N being Avogadro's number and k the Boltzmann constant) in the lower panel of Figure 2. They were numerically fitted, by use of the simplex algorithm,[19] to the axially anisotropic spin-Hamiltonian (2), by numerical diagonalisation of the full spin-Hamiltonian matrix.

$$\hat{H} = -2J\hat{S}_1 \cdot \hat{S}_2 + \sum_{i=1,2}\{\mu_B \vec{B} g \hat{S}_i + D[\hat{S}_{z,i}^2 - S_i(S_i+1)/3]\} \qquad (2)$$

Here D is the uniaxial anisotropy, and $S = 2$ the total spin of the Mn(III) ions. The best fit D parameter, keeping J fixed to J = +1.24 cm^{-1} (as determined by fitting the $\chi_M T$ product of **1**), was D = - 3.64 cm^{-1}.

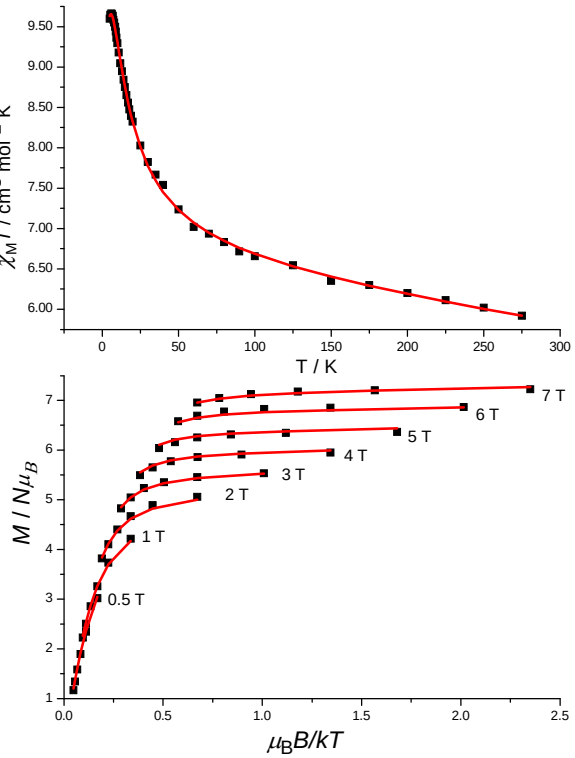

Figure 2 Upper panel: Plot of the $\chi_M T$ product of **1** vs. T in the 275 - 5 K temperature range in an applied field of 0.1 T. The solid red line is the best-fit of the data with J = +1.24 cm^{-1} and g = 2.0. Lower panel: Plot of reduced magnetisation in the 2.0 to 7.0 K temperature range and at the indicated field strengths. The solid red lines are the best-fit of the data with J = +1.24 cm^{-1}, g = 2.0 and D = -3.64 cm^{-1}. See text for details.

EPR Spectroscopy

High-frequency Electron Paramagnetic Resonance (HFEPR) data were collected for complex **1** on a finely ground powder sample (41.2 mg) pressed into a KBr pellet (102 mg) in order to avoid field-alignment of the micro-crystallites within the powder. Measurements were performed in the temperature range 2.5 to 30 K and at high-frequencies between 100 and 430 GHz. The HFEPR spectra were obtained using a broadband transmission-type probe that employs cylindrical light-pipes;[21] microwaves were generated using a phase-locked Virginia Diodes solid-state source operating at 13±1 GHz, followed by a chain of multipliers. High magnetic fields were provided by an Oxford Instruments superconducting magnet.

Figure 3 separately displays the temperature dependence of parallel ($B//z$) and perpendicular ($B\perp z$) components of representative powder spectra obtained for complex **1**. Due to the significant zero-field splitting experienced by **1**, these two measurements were performed at quite different frequencies (406.4 (a) and 165.6 GHz (b) for z and xy, respectively) in order to match the most prominent features to the available field window. For an easy-axis (D < 0) system at low temperatures, one expects the strongest parallel components to occur on the low-field side of the g = 2.00 position (indicated in both panels of Fig. 3), while the stronger perpendicular components should occur on the high-field side, as is clearly the case in Fig. 3.

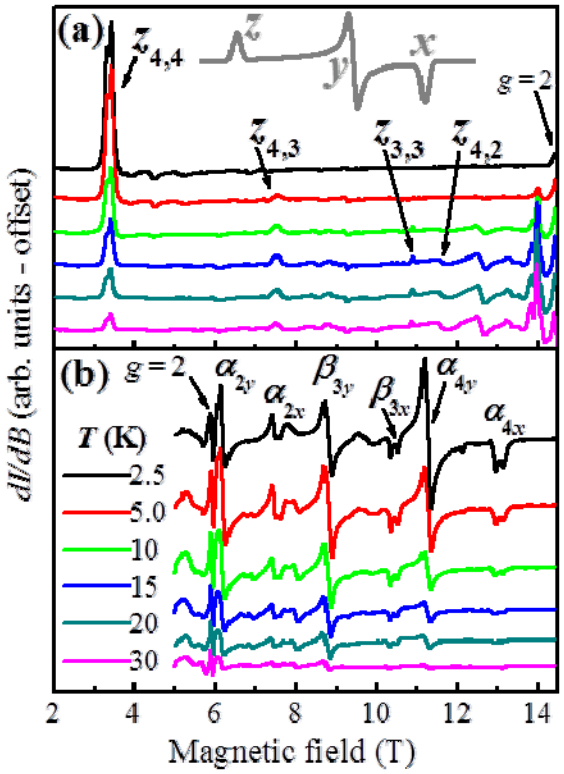

Figure 3 Temperature dependent powder HFEPR spectra recorded in field derivative mode in the temperature range from 2.5 to 30 K: the measurements in (a) were recorded at 406.4 GHz, emphasizing the parallel ($B//z$) components of the spectrum; those in (b) were recorded at 165.6 GHz, emphasizing the perpendicular ($B\perp z$) components. The main resonance features are labeled according to the scheme described in the main text. The inset (top) depicts a typical T = 0 derivative mode powder spectrum for a biaxial system, illustrating the lineshapes expected for the x, y and z components of the spectrum.

The spectra were recorded in field-derivative mode (dI/dB, where I denotes the absorption intensity), making it relatively straightforward to determine which peaks correspond to which components of the spectrum. The inset to Fig. 3(a) displays a trivial example of a T = 0 derivative mode powder spectrum for a biaxial system for which three features are observed: the z-component corresponds to the onset of absorption and appears as a peak in the derivative; the x component corresponds to the cessation of absorption and thus appears as a dip in the derivative; meanwhile, the y component occurs at the maximum in absorption and therefore looks like the derivative of the z-component. Examination of the first few resonances in Fig. 3(a) indicates that they are indeed peaks, confirming their assignment to the parallel part of the spectrum. However, the resonances

change to more of a derivative shape as the centre ($g = 2$) position of the spectrum is approached.

Based on simulations (*vide infra*), the peaks in Fig. 3(a) have been labeled according to the notation $z_{S,ms}$, where S denotes the spin multiplet state associated with the excitation, and m_S denotes the magnitude of the spin projection associated with the state from which the transition was excited. Accordingly, the strongest low-temperature peak is $z_{4,4}$ corresponding to the lowest-lying m_S = - 4 to - 3 excitation associated with the S = 4 ground state multiplet. We note that, as the temperature is increased, many more features emerge in the spectrum, especially as one approaches the isotropic $g = 2.00$ position. It is possible to assign many of these features to transitions within excited spin multiplet states (*vide infra*), e.g., $z_{3,3}$. Finally, we note that the strongest peak in Fig. 3(a) displays fine structures that are most likely attributable to multiple molecular microenvironments with slightly different *zfs* parameters.[22] Such strains are very common in molecular clusters and we shall see similar evidence for such behavior in the perpendicular spectra.[22-25]

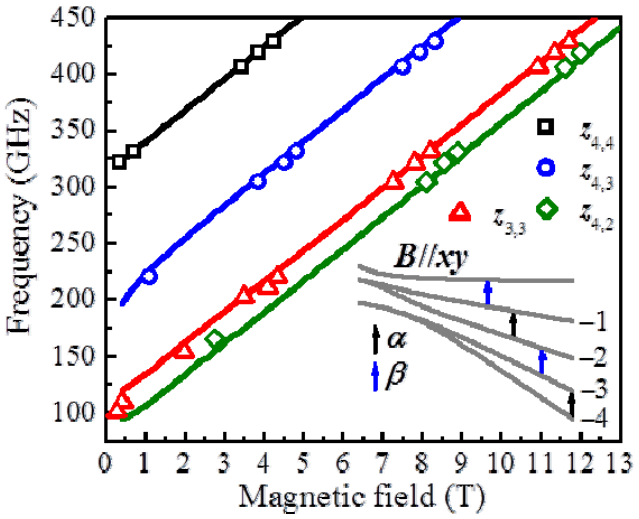

Figure 4 Frequency dependence of the main HFEPR peak positions (see main text for explanation of labeling) determined from parallel spectra such as those in Fig. 3(a). The solid curves represent the best simulation of the data according to the Hamiltonian of Eqn. (3). The lower right inset depicts the perpendicular Zeeman diagram, illustrating the origin of the α and β resonances seen in Fig. 3(b) and Fig. 5 (see main text for further explanation).

Figure 3(b) clearly contains two distinct types of excitation: those observed as double dips, which we assign to the x components, and those that appear as derivatives, which we assign to the y components. The two dips in the x-component spectrum again suggest multiple microenvironments. The resonances in Fig. 3(b) have been labeled according to a scheme developed previously for the Mn_{12} SMM.[23] At the lowest frequencies, the excitations may be further grouped into two types, α and β, depending on whether they occur between pairs of levels that are nearly degenerate (α), or separated by a gap (β) in zero field. This is illustrated in the inset to Fig. 4, which shows the perpendicular ($B//xy$) Zeeman diagram associated with the low-energy portion of the S = 4 ground state, and where the α and β transitions are indicated with black and blue arrows, respectively. This distinction will become important below when we attempt to simulate the powder spectra. The resonances in Fig. 3(b) are thus labeled either α or β, with subscripts that denote (i) the approximate m_S value (even for α and odd for β) associated with the state from which the transition was excited, and (ii) whether the excitation belongs to the x or y part of the spectrum. The m_S values are only exact in the very high-field/frequency limit in which the quantisation axis is determined by the applied magnetic field vector.

Figure 4 plots the positions of main peaks observed in the parallel spectra determined from measurements spanning a wide range of high-frequencies, while Fig. 5 displays similar plots corresponding to the perpendicular spectra. Included in the Figures are the best simulations (solid curves) of the combined data sets employing the anisotropic spin-Hamiltonian (3):

$$\hat{H} = -2J\hat{S}_1 \cdot \hat{S}_2 + \sum_{i=1,2}\{\mu_B \vec{B} g \hat{S}_i + D[\hat{S}_{z,i}^2 - S_i(S_i+1)/3] + E(\hat{S}_{x,i}^2 - \hat{S}_{x,i}^2)\} \qquad (3)$$

where E is the rhombic anisotropy parameter associated with the Mn^{III} ions. One of the major advantages of performing multi-frequency measurements is that different features in the combined data sets separately constrain each of the free parameters in the above Hamiltonian.[26] To start with, we have previously argued[27] that, for a ferromagnetic molecule with parallel D tensors, the zero-field intercept (*zfs*) associated with the parallel ground state transition ($z_{4,4}$ in Fig. 4) depends only on D, i.e., it is completely insensitive to any of the other parameters in the above Hamiltonian. Given that this is the most prominent feature in the entire study, we use it to fix D. The locations of the 2nd and 3rd ground state parallel resonances ($z_{4,3}$ and $z_{4,2}$ in Fig. 4) then constrain J, while the slopes of the lines in Fig. 4 constrain the z-component of the g tensor. The effect of J is to introduce higher ($> 2^{nd}$) order interactions into the effective description of the S = 4 ground state (not considered here) that result in uneven field spacing of the corresponding resonance branches. This is clearly the case in Fig. 4, and it is this uneven spacing (i.e. the locations of $z_{4,3}$ and $z_{4,2}$ relative to $z_{4,4}$) that constrains J.

We next turn to the perpendicular spectra in Fig. 5. Introduction of a rhombic E term together with a tuning of the x and y components of the Landé g-tensor produces near perfect agreement in terms of the α resonances (thick black curves). The rhombic interaction effectively splits the x and y components, shifting the former (latter) to higher (lower) fields, while the g values again determine the slopes. The only remaining issue concerns the low-frequency behavior of the β resonances (blue data points), which deviate dramatically from x and y component expectations (thick blue curves).

The low-frequency behaviour of the β resonances is not new, having been documented previously by other authors[29-31] as well as by some of the authors of the present study for the case of Mn_{12}.[23] The simple 2nd order Hamiltonian above possesses D_{2h} symmetry. In the strict high field limit ($B >> DS/g\mu_B$), it gives rise to resonant (EPR) excitations that have turning points when the field is applied along each of the three principal Cartesian axes x, y and z, i.e., when rotating in one of the three Cartesian

planes (*xy*, *yz* or *zx*), the field location of each resonance will oscillate from a minimum to a maximum, with the extrema (turning points) located exactly along the Cartesian axes. It is these turning points that dominate the powder derivative spectrum. However, if the high field criterion is not met, these turning points need not necessarily lie along the Cartesian axes. This can give rise to what are termed 'off-axis resonances' in powder measurements at low frequencies.[23,29-31] This is precisely the explanation for the low frequency behaviour of the β resonances, and very similar effects have been observed in Mn_{12}.[23,32]

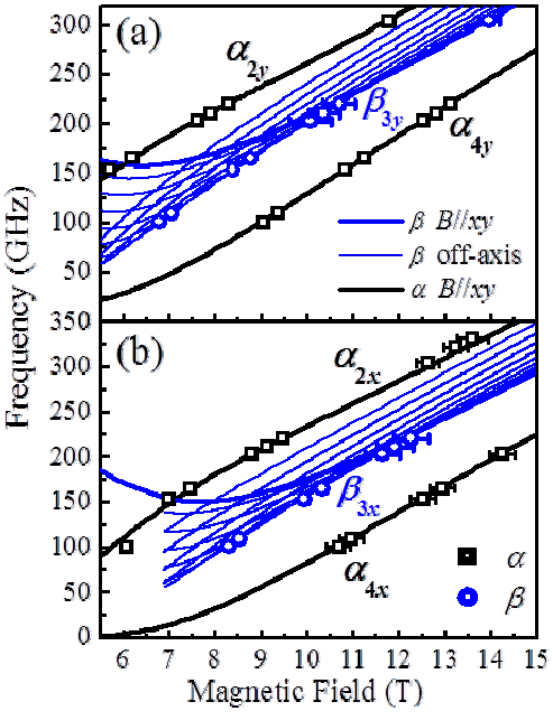

Figure 5 Frequency dependence of the main HFEPR peak positions (see main text for explanation of labeling) determined from *x* (a) and *y* (b) components of spectra such as those displayed in Fig. 3(b). The thick solid curves represent the best simulation of the α (black) and β (blue) resonances according to the spin-Hamiltonian of Eqn. (3). The thin blue curves correspond to simulations with the field applied away from the *xy*-plane (in 2° increments); these curves account for the low-frequency off-axis β resonances (see main text for further explanation).

To demonstrate the above assertion, we include additional simulations in Fig. 5, corresponding to field orientations away from the *xy* plane in 2° increments (thin blue curves). At the highest frequencies, the off-axis curves all occur to the low-field side of the *B*//*xy* curve (thick blue line), i.e., the turning points lie exactly along *x* and *y*. However, at the lowest frequencies, the simulations move initially to higher fields, but then retreat again to lower fields, i.e., as expected the turning points lie out of the *xy* plane. The field orientations corresponding to the turning points (maximum field) are frequency dependent. Nevertheless, by plotting a series of such curves, one indeed finds that they tend to the locations of the observed low-frequency β resonances. In other words, a single parameterisation accounts perfectly for all aspects of the powder measurements. The optimum simulation parameters are: D = - 3.49 cm^{-1}, $|E|$ = 0.16 cm^{-1}, J = +1.17 cm^{-1} (ferromagnetic) and g = 2.00.

Finally, we comment on the obtained parameters. There is excellent agreement between the single-ion uniaxial anisotropy and isotropic exchange parameters obtained from the HFEPR measurements and the fitting of the susceptibility and reduced magnetisation data (D = - 3.64 cm^{-1}, J = +1.24 cm^{-1}). EPR studies are normally insensitive to exchange. However, as we have recently shown, one can indirectly determine J rather precisely in the case of simple clusters for which the exchange is comparable to, or weaker than the anisotropy associated with the constituent ions.[26] This condition clearly applies for the present example, again illustrating the utility of HFEPR for such studies. We note that the obtained value for D is exactly in the same range of -3.4 to -3.6 cm^{-1} as found for many related Mn^{III} complexes.[10,15,25,27,28]

Theoretical Analysis

All calculations were performed with version 2.8 of the program ORCA,[33] with the *TZVP* basis set proposed by Ahlrichs used in all cases.[34,35] For density functional theory (*DFT*) calculations, *resolution of the identity* (*RI*) approximation with the auxiliary *TZV/J* Coulomb fitting basis sets were employed.[36] For *Complete Active Space* (*CAS)* calculations, these were replaced by *TZV/C*.[37-39] In certain cases, the electronic effects of the acetonitrile solvent were introduced via the *conductor-like screening model* (*COSMO*).[40] *DFT* calculations on the zero-field splitting (*zfs*) were carried out using the coupled perturbed and Pederson-Khanna methods, as well as quasi-restricted theory.[41,42] The spin-orbit and spin-spin coupling operators employed are based in the *SOMF* scheme.[42] Models A and B (Figure 6) were built from the experimental molecular geometry of the dinuclear complex (Figure 6). In Model A one Mn^{III} ion has been replaced by a diamagnetic Zn^{II} ion, and in Model B the molecule has been cleaved in half to produce a mononuclear Mn^{III} complex. Contributions to the axial (*D*) and rhombic (*E*) magnetic anisotropy from second-order spin-orbit and spin-spin coupling were calculated from methods based on *density-functional theory* (*DFT*) and post-Hartree-Fock methods based on the *CAS* treatment,[42] and used as implemented in ORCA. Those based on *DFT* calculations were incorporated by means of mean-field approximations. The choice of conditions for the calculations was made using a combination of literature precedents and tests performed by us using different functionals (including hybrid functionals) and different methods to calculate the spin-orbit coupling [*coupled perturbed*, *quasi-restricted* (*QRO*) and *Pederson-Khanna* techniques] in the complex [Mn(bpea)F_3] (bpea = N,N-bis(2-pyridylmethyl)-ethylamine).[41-44] Results with the *BLYP* functional and *QRO* technique provide *D* values closest to experiment and therefore they will be the only ones presented in the manuscript. The chosen active space in *CAS* was composed of the five manganese *d* orbitals occupied by four electrons, with the diagonalised *SOC* matrix derived from the 5 lowest quintet and 35 lowest triplet states.

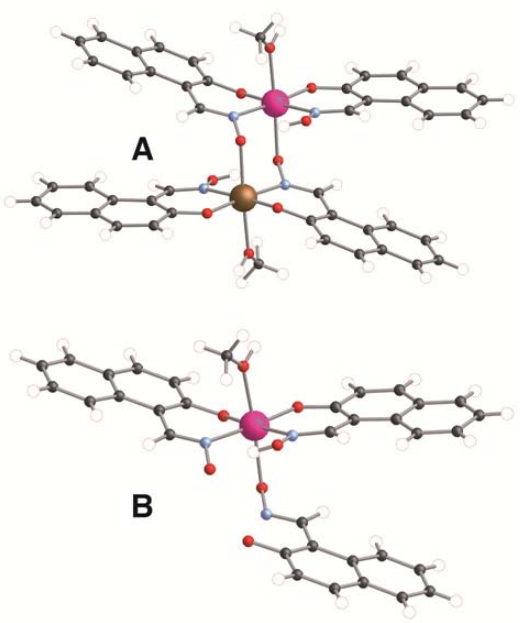

Figure 6. Model A (top) and model B (bottom) constructed from the crystal structure of **1**. Colour code, Mn = pink; Zn = brown; N = blue; O = red; C = grey; H = white.

High-spin Mn^{III} ions possess a d^4 electronic configuration with a quintuplet ground state. The Jahn-Teller effect results in one of the e_g orbitals being unoccupied and non-magnetic. In axially-elongated complexes this is the x^2-y^2 orbital, and in axially compressed complexes this is the z^2 orbital. This is normally reflected in negative and positive values of the axial magnetic anisotropy (*D*) parameter, respectively. However, in some cases distributions in the metal-ligand bond lengths, which is particularly relevant when a variety of donor atoms are present in the coordination sphere, does not permit such a simple analysis. Complex **1** is indeed such a case. In these situations, calculations of the electronic structure provide invaluable support. In the present work both *DFT* and *CAS* methods have been employed in order to evaluate the contributions to the axial (*D*) and rhombic (*E*) magnetic anisotropy, originating from the spin-orbit and spin-spin coupling. The results from calculations performed on Models A and B are summarised in Table 1.

As has been observed in previous studies, better agreement with experiment was found from *CASSCF* calculations; albeit with a slight overestimation of the *D* parameter in some cases.[44] Results based on *DFT* and *CAS* calculations provide negative values for the *D* parameter that correspond to an axially elongated molecular geometry. In model **B**, *DFT* calculations provide a positive value of *D*. However, inclusion of the electronic effects from neighbouring molecules propagated via the acetonitrile results in an inversion of sign (see values in parentheses in Table 1). These new values are close to that found in Model **A,** in the presence or absence of solvent. Since *DFT* calculations tend to overestimate electron delocalisation, molecules in which (highly) negatively charged ligands are coordinated to the (positively charged) metal ions can be somewhat unstable, causing partial charge transfers or the inversion of the e_g magnetic orbital. This can be avoided through the inclusion of an adaptable cavity with a dielectric constant that allows for simulation of the intermolecular electronic interactions, stabilising the surplus electronic density on the ligands.[45-47] Even if the spin-orbit contribution is predominant, the spin-spin contribution is non-negligible and must be considered in the quantitative evaluation of the *D* parameter.[44]

Table 1 Calculated values of *D* (cm^{-1}), its components (spin-spin, D_{SS}; spin-orbit, D_{SO}), and *E* / *D* ratio for Models **A** and **B** using *DF* (*BLYP* functional and *QRO* method) and *CAS* techniques. The values in parentheses are those found when solvent effects are included through the *COSMO* approach.

	Model A		Model B	
	BLYP	CAS	BLYP	CAS
D_{SO}	–2.25	–3.56	+2.85 (–2.29)	–3.22
D_{SS}	–0.38	–0.50	+0.41 (–0.39)	–0.47
D	–2.63	–4.04	+3.25 (–2.68)	–3.69
E / *D*	0.129	0.071	0.187 (0.185)	0.096

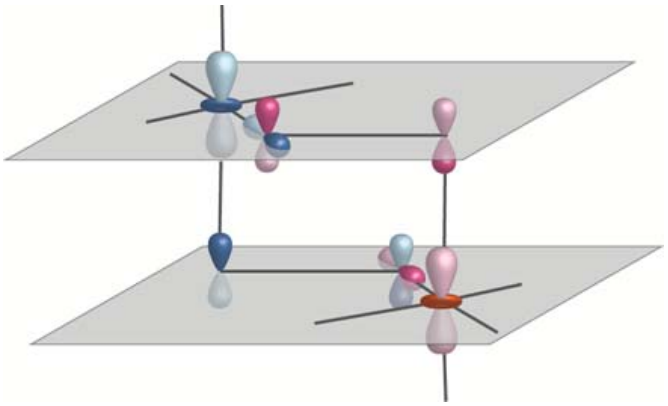

Figure 7. Schematic view of the orthogonality between the magnetic orbitals, which are displayed in different colours (blue and red) for each metal centre. The electronic densities delocalised for each Mn^{III} ion meet at the nitrogen atoms in an orthogonal fashion.

The nature and magnitude of the magnetic coupling were also examined using *DFT* calculations on the nonet and broken-symmetry singlet spin states of **1**, resulting in a weak ferromagnetic coupling constant ($J = +0.5$ cm^{-1}) between the two paramagnetic quintet Mn^{III} ions, in excellent agreement with the experimental data. As suggested in previous work by us, the nature of pairwise magnetic coupling can be explained by an accidental orthogonality between the Mn-N-O plane of the first Mn^{III} ion and the Jahn-Teller axis of the second Mn^{III} ion (Figure 7).[15] The result is no overlap between z^2 orbitals on adjacent metal ions which are only able to delocalise electron density through the σ-pathway.

Conclusions

The reaction between $MnCl_2 \cdot 4H_2O$, Naphth-saoH_2 and NaOMe in MeOH affords crystals of the dimetallic cluster compound $[Mn^{III}_2(Naphth\text{-}sao)_2(Naphth\text{-}saoH)_2(MeOH)_2]$•4MeOH (1•4MeOH). Complex **1** is a symmetric dimer with a very simple $[Mn\text{-}O\text{-}N\text{-}Mn]_2$ magnetic core, allowing it to be an excellent and

simple model complex with which to examine the magneto-structural relationship. SQUID magnetometry reveals weak ferromagnetic exchange mediated through the heavily twisted Mn-O-N-Mn moiety, with high field, high frequency EPR data determining a single ion anisotropy, $D_{(MnIII)}$ = -3.94 cm^{-1}. Theoretical studies afford calculated values of the exchange coupling and the anisotropy that are in excellent agreement with both SQUID and EPR experiments, and suggest that the weak ferromagnetism results from an accidental orthogonality between the Mn-N-O plane of one Mn^{III} ion and the Jahn-Teller axis of the other.

Acknowledgements

LFJ acknowledges the IRCSET Embark Fellowship Program for funding EH. EKB wishes to thank the Leverhulme Trust and the EPSRC. JC acknowledges the financial support of the Spanish Ministerio de Ciencia e Innovación through projects CTQ2010-15364, Molecular Nanoscience (Consolider Ingenio CSD2007-00010) and Generalitat Valenciana (PROMETEO/2009/108). Work at the National High Magnetic Field Laboratory is supported by NSF Cooperative Agreement No. DMR-0654118 and by the State of Florida. SH acknowledges the support of the NSF (CHE0924374) and SP the Danish Natural Science Research Council (FNU) for a Sapere Aude Fellowship (10-081659). AGR would like to thank Mr. Harry Owen and Kaiser Optical Systems Inc. for the provision of the Raman instrumentation used in this study.

Notes and references

[a]*School of Chemistry, NUI Galway, University Road, Galway, Ireland. E-mail: leigh.jones@nuigalway.ie, alan.ryder@nuigalway.ie*
[b]*EaStCHEM School of Chemistry, The University of Edinburgh, The Kings Buildings, West Mains Road, Edinburgh, EH9 3JJ, UK. Tel: +44 (0)131-650-7545; E-mail: ebrechin@staffmail.ed.ac.uk*
[c]*National High Magnetic Field Laboratory and Department of Physics, Florida State University, 1800 E. Paul Dirac Drive, Tallahassee, FL 32310, USA. E-mail: shill@magnet.fsu.edu*
[d]*Instituto de Ciencia Molecular (ICMol) and Fundació General de la Universitat de València (FGUV), Catedrático José Beltrán nº 2, Universitat de València, E-46980 Paterna, València, Spain*
[e]*Department of Chemistry, University of Copenhagen, Universitetsparken 5, DK-2100, Denmark. E-mail: piligkos@kiku.dk*

1 D. Gatteschi, O. Kahn and R. D. Willet, Eds. *Magneto-Structural Correlations in Exchange-Coupled Systems*; D. Reidel: Dordrecht, 1985.
2 W. E. Hatfield, *Comments Inorg. Chem*., 1981, **1**, 105.
3 J. Glerup, D. J. Hodgson and E. Petersen, *Acta Chem. Scand.,* 1983, **A37**, 161.
4 D. Gatteschi and R. Sessoli, *Angew. Chem.*, *Int. Ed.,* 2003, **42**, 268.
5 G. A. Timco, T. B. Faust, F. Tuna and R. E. P. Winpenny, *Chem. Soc. Rev*., 2011, **40**, 3067.
6 M. Evangelisti and E. K. Brechin, *Dalton Trans*., 2010, **39**, 4672.
7 See for example: J. Schnack, M. Luban and R. Modler, *Europhys. Lett*., 2001, **56**, 863.
8 See for example: G. Aromí and E. K. Brechin, *Struct. Bonding*, 2006, **122**, 1.
9 A. G. Smith, P. A. Tasker and D. J. White, *Coord. Chem. Rev*., 2003, **241**, 61.
10 (a) R. Inglis, S. M. Taylor, L. F. Jones, G. S. Papaefstathiou, S. P. Perlepes, S. Datta, S. Hill, W. Wernsdorfer and E. K. Brechin, *Dalton Trans*., 2009, 9157. b) R. Inglis, L. F. Jones, C. J. Milios, S. Datta, A. Collins, S. Parsons, W. Wernsdorfer, S. Hill, S. P. Perlepes, S. Piligkos and E. K. Brechin, *Dalton Trans*., 2009, 3403. c) R. Inglis, A. D. Katsenis, A. Collins, F. White, C. J. Milios, G. S. Papaefstathiou and E. K. Brechin, *CrystEngComm*., 2010, **12**, 2064.
11 R. Dunsten and T. A. Henry, *J. Chem. Soc. Trans*., 1899, **75**, 66.
12 G. M. Sheldrick, *Acta. Crystallogr., Sect. A: Found. Crystallogr.,* 1990, **A46**, 467.
13 G. M. Sheldrick, SHELXL-97, A computer programme for crystal structure determination, University of Gottingen, 1997.
14 P. McArdle, P. Daly and D. Cunningham, *J. Appl. Crystallogr*., 2002, **35**, 378.
15 R. Inglis, E. Houton, J. Liu, A. Prescimone, J. Cano, S. Piligkos, S. Hill, L. F. Jones and E. K. Brechin, *Dalton Trans*., 2011, **40**, 9999.
16. G. Socrates. *Infra-Red and Raman Characteristic Group Frequencies.* (2004) Wiley VCH Publishing.
17. F. Birkelbach, M. Winter, U. Flörke, H.-J. Haupt, C. Butzlaff, M. Lengen, E. Bill, A. X. Trautwein, K. Wieghardt and P. Chaudhuri. *Inorg. Chem.,* 1994, **33**, 3990-4001.
18. (a) C. Papatriantafyllopoulou, G. Aromi, A. J. Tasiopoulos, V. Nastopolos, C. P. Raptopoulou, S. J. Teat, A. Escuer and S. P. Perlepes. *Eur. J. Inorg. Chem.,* 2007, 2761-2774. (b) T. Weyhermüller, R. Wagner, S. Khandra and P. Chaudhuri. *Dalton Trans.,* 2005, 2539-2546. (c) P. Chaudhuri, M. Winter, U. Flörke and H.-J. Haupt. *Inorg. Chim. Acta.,* 1995, **232**, 125-130.
19 W. H. Press, S. A. Teukolsky, W. T. Vetterling, B. P. Flannery, *"Numerical Recipes in C: The Art of Scientific Computing"*. Second Edition, Cambridge, Cambridge University Press, 1992.
20 C. J. Milios, R. Inglis, A. Vinslava, R. Bagai, W. Wernsdorfer, S. Parsons, S. P. Perlepes, G. Christou and E. K. Brechin, *J. Am. Chem. Soc*., 2007, **129**, 12505.
21 A. K. Hassan, L. A. Pardi, J. Krzystek, A. Sienkiewicz, P. Goy, M. Rohrer and L. C. Brunel, *J. Mag. Res*., 2000, **142**, 300.
22 (a) S. Hill, R. S. Edwards, S. I. Jones, J. M. North and N. S. Dalal, *Phys. Rev. Lett*., 2003, **90**, 217204. (b) For general reading on this subject see also: J. R. Pilbrow. Transition Ion Electron Paramagnetic Resonance. *Oxford Science Publications.* Clarendon Press. 1990.
23 S. Takahashi, R. S. Edwards, J. M. North, S. Hill and N. S. Dalal, *Phys. Rev. B*, 2004, **70**, 094429.
24 J. Lawrence, E.-C. Yang, R. Edwards, M. M. Olmstead, C. Ramsey, N. S. Dalal, P. K. Gantzel, S. Hill and D. N. Hendrickson, *Inorg. Chem*., 2008, **47**, 1965.
25 R. Inglis, L. F. Jones, C. J. Milios, S. Datta, A. Collins, S. Parsons, W. Wernsdorfer, S. Hill, S. P. Perlepes, S. Piligkos and E. K. Brechin, *Dalton Trans*, 2009, 3403.
26 J. Lawrence, S. Hill, E.-C. Yang and D. N. Hendrickson, *Phys. Chem. Chem. Phys*., 2009, 6743.
27 S. Hill, S. Datta, J. Liu, R. Inglis, C. J. Milios, P. L. Feng, J. J. Henderson, E. del Barco, E. K. Brechin, D. N. Hendrickson, Perspectives Article in Themed Issue, Dalton Trans. **39**, 4693-4707 (2010).
28. B. J. Kennedy and K. S. Murray. *Inorg. Chem.,* 1985, **24**, 1552-1557.
29 Y. Teki, T. Takui and K. Itoh, *J. Chem. Phys*., 1988, **88**, 6134.
30 P. Bearwood, D. M. L. Goodgame and R. E. P. Winpenny, *J. Chem. Phys*., 1989, **90**, 3401.
31 R. R. Rakhimov, A. L. Wilkerson, G. B. Loutts and H. R. Reis, *J. Appl. Phys*., 1997, **82**, 1970.
32 E. del Barco, A. D. Kent, S. Hill, J. M. North, N. S. Dalal, E. M. Rumberger, D. N. Hendrickson, N. Chakov and G. Christou, *J. Low Temp. Phys.*, 2005, **140**, 119.
33 F. Neese, *Wires Comput. Mol, Sci.,* 2012, **2**, 73.
34 A. Schafer, H. Horn and R. Ahlrichs, *J. Chem. Phys.,* 1992, **97**, 2571.
35 A. Schafer, C. Huber and R. Ahlrichs, *J. Chem. Phys.,* 1994, **100**, 5829.
36 R. A Kendall and H. A. Fruchtl, *Theor. Chem. Acc.,* 1997, **97**, 158.
37 K. Eichkorn, O. Treutler, H. Ohm, M. Haser and R. Ahlrichs, *Chem. Phys. Lett.,* 1995, **240**, 283.
38 K. Eichkorn, O. Treutler, H. Ohm, M. Haser and R. Ahlrichs, *Chem. Phys. Lett.,* 1995, 242, 652.
39 K. Eichkorn, F. Weigend, O. Treutler and R. Ahlrichs, *Theor. Chem. Acc.* 1997, **97**, 19.

40 A. Klamt and G. Schuurmann, *J. Chem. Soc. Perkin Trans. 2,* 1993, 799.
41 M. R. Pederson and S. N. Khanna, *Phys. Rev. B,* 1999,60, 9566.
42 F. Neese, *J. Am. Chem. Soc.,* 2006, **128**, 10213.
43 F. Neese, *J. Chem. Phys.,* 2007, 127, 164112.
44 C. Duboc, D. Ganyushin, K. Sivalingam, M. Collomb and F. Neese, *J. Phys. Chem. A,* 2010, **114**, 10750.
45 D. Visinescu, L. M. Toma, J. Cano, O. Fabelo, C. Ruiz-Perez, A. Labrador, F. Lloret and M. Julve, *Dalton Trans,* 2010, **39**, 5028.
46 S. Nastase, C. Maxim, M. Andruh, J. Cano, C. Ruiz-Perez, J. Faus, F. Lloret and M. Julve, *Dalton Trans.,* 2011, **40**, 4898.
47 J. Vallejo, I. Castro, M. Déniz, C. Ruiz-Pérez, F. Lloret, M. Julve, R. Ruiz-García and J. Cano, *Inorg. Chem.,* 2012, **51**, 3289.